Photosynthesis Research
https://doi.org/10.1007/s11120-021-00834-2

ORIGINAL ARTICLE

Photoelectrochemistry of metalloporphyrin-modified GaP semiconductors

Daiki Nishiori[1] · Brian L. Wadsworth[1] · Edgar A. Reyes Cruz[1] · Nghi P. Nguyen[1] · Lillian K. Hensleigh[1] · Timothy Karcher[2] · Gary F. Moore[1]

Received: 4 November 2020 / Accepted: 9 April 2021

Abstract

Photoelectrosynthetic materials provide a bioinspired approach for using the power of the sun to produce fuels and other value-added chemical products. However, there remains an incomplete understanding of the operating principles governing their performance and thereby effective methods for their assembly. Herein we report the application of metalloporphyrins, several of which are known to catalyze the hydrogen evolution reaction, in forming surface coatings to assemble hybrid photoelectrosynthetic materials featuring an underlying gallium phosphide (GaP) semiconductor as a light capture and conversion component. The metalloporphyrin reagents used in this work contain a 4-vinylphenyl surface-attachment group at the β-position of the porphyrin ring and a first-row transition metal ion (Fe, Co, Ni, Cu, or Zn) coordinated at the core of the macrocycle. In addition to describing the synthesis, optical, and electrochemical properties of the homogeneous porphyrin complexes, we also report on the photoelectrochemistry of the heterogeneous metalloporphyrin-modified GaP semiconductor electrodes. These hybrid, heterogeneous-homogeneous electrodes are prepared via UV-induced grafting of the homogeneous metalloporphyrin reagents onto the heterogeneous gallium phosphide surfaces. Three-electrode voltammetry measurements performed under controlled lighting conditions enable determination of the open-circuit photovoltages, fill factors, and overall current–voltage responses associated with these composite materials, setting the stage for better understanding charge-transfer and carrier-recombination kinetics at semiconductor|catalyst|liquid interfaces.

Keywords Artificial photosynthesis · Photoelectrochemistry · Molecular-modified photocathodes · Metalloporphyrins · Gallium phosphide · Hydrogen evolution

Introduction

Photosynthesis offers inspiration for imagining and developing renewable energy technologies that use sunlight to produce fuels and other value-added chemical products (Vullev 2011; Faunce et al. 2013). One approach to achieving such technologies includes the direct integration of light-harvesting semiconductors with electrocatalysts for storing energy in chemical form. The effective operation of these modified electrodes can be described via four discrete steps, including: (1) the absorption of light by the semiconductor to create electron–hole pairs, (2) the separation of charges within the semiconductor to deliver charge carriers to semiconductor|catalyst interfaces, (3) the injection of charges across semiconductor|catalyst interfaces to advance the redox states of catalytic sites, and (4) the generation of fuels at catalyst|liquid interfaces. Despite differences in the details of how charges move through these human-engineered assemblies, the overall steps have conceptual parallels with those at play in the biological process of photosynthesis. As in the case of natural photosynthesis, there is also an incomplete understanding of the operating principles that govern these artificial photosynthetic constructs. Thus, developing effective strategies for interfacing catalysts with light-absorbing materials remains challenging (McKone et al. 2014; Ardo et al. 2018). Although efforts focused on overall system efficiency have been insightful, an improved understanding of the fundamental kinetics and

✉ Gary F. Moore
gary.f.moore@asu.edu

[1] School of Molecular Sciences and the Biodesign Institute Center for Applied Structural Discovery (CASD), Arizona State University, Tempe, AZ 85287-1604, USA

[2] Eyring Materials Center, Arizona State University, Tempe, AZ 85287-8301, USA

Published online: 22 May 2021

thermodynamics governing how charges move through these materials is critical to developing rational synthetic schemes for improving their performance.

In this article, we describe the synthesis and photoelectrosynthetic properties of metalloporphyrin-modified gallium phosphide (GaP) electrodes. These hybrid assemblies are prepared via UV-induced grafting of metalloporphyrin analogs bearing a 4-vinylphenyl surface-attachment group at the β-position of the macrocycle. Metalloporphyrins have a relatively rich history as catalysts for the hydrogen evolution reaction (HER) (Beyene and Hung 2020) as well as oxygen reduction, carbon dioxide reduction, and oxygen evolution reactions (Zhang et al. 2017; Gotico et al. 2020). In contrast to a synthetic method previously reported by our research group, utilizing the coordination of cobalt porphyrin catalysts to nitrogen sites of an initially photo-grafted polymeric interface (Beiler et al. 2017), the one-step grafting method described herein does not rely on the coordination chemistry of a specific metal center. This approach enables functionalization of (semi)conducting materials with metal centers that were previously inaccessible. The metalloporphyrin analogs used in this study include Fe, Co, Ni, Cu, or Zn metal centers, where the Ni, Cu, and Zn porphyrins are novel compounds. The synthesis and characterization of the Fe and Co analogs have been previously reported by our group (Khusnutdinova et al. 2017) and are included in this report to facilitate comparisons. In addition to providing details on the optical and electrochemical properties of the homogeneous metalloporphyrin reagents, photoelectrochemical properties of the metalloporphyrin-modified photocathodes, including current–voltage responses measured under simulated solar illumination in pH-neutral aqueous solutions, are also included. All photoelectrochemical studies were performed using three-electrode measurements featuring metalloporphyrin-modified GaP working electrodes and appropriate counter as well as reference electrodes. The open-circuit photovoltage (V_{oc}), short-circuit current density (J_{sc}), maximum power point (P_{max}), and fill factor (*ff*) recorded using each metalloporphyrin-modified semiconductor electrode are discussed in the context of limitations associated with light capture and conversion properties of the underlying semiconductor, band bending effects within the semiconductor, surface recombination kinetics, and catalysis.

Materials and methods

Materials

All reagents were purchased from Aldrich or Thermo Fisher Scientific. Solvents were obtained from Aldrich, VWR or Thermo Fisher Scientific. Dichloromethane, hexanes, toluene, methanol, pyridine, dimethylformamide, and *p*-tolualdehyde were freshly distilled before use. Milli-Q water (18.2 MΩ cm) was used to prepare all aqueous solutions. Single crystalline p-type, Zn-doped GaP(100) wafers were purchased from the Institute of Electronic Materials Technology and were single-side polished to an epi-ready finish. The GaP(100) wafers have a resistivity of 1.35×10^{-2} Ω cm and a carrier concentration of 7.07×10^{17} cm^{-3}, with an etch pit density of less than 2×10^4 cm^{-2}. The GaP ingot used to prepare the samples described in this report has different physical characteristics (doping density, charge mobility, and resistance) than those used in previous studies from our group (Cedeno et al. 2014; Krawicz et al. 2014; Beiler et al. 2016, 2017; Khusnutdinova et al. 2017).

Instrumentation

Ultraviolet–Visible (UV–Vis) optical spectra were recorded on a Shimadzu SolidSpec-3700 spectrometer with a D_2 (deuterium) lamp for the ultraviolet range and a WI (halogen) lamp for the visible and near-infrared. Mass spectra of all compounds were obtained with Voyager DE STR matrix-assisted laser desorption/ionization time-of-flight (MALDI-TOF) mass spectrometer in positive ion mode employing a *trans,trans*-1,4-diphenyl-1,3-butadiene matrix. Nuclear magnetic resonance (NMR) spectra were recorded on a Bruker Avance NEO 500 MHz spectrometer or Varian MR400 spectrometer operating at 400 MHz. Fourier transform infrared (FTIR) spectra were collected in pressed KBr pellets using a transmission mode with a 1 cm^{-1} resolution, and the data were processed using OPUS software. Background measurements were obtained from the air, and baselines were corrected for rubberband scattering. X-ray photoelectron spectroscopy (XPS) was performed using a monochromatized Al Ka source ($h\nu = 1486.6$ eV), operated at 63 W, on a VG ESCALAB 220i-XL (Thermo Fisher) system at a takeoff angle of 0° relative to the surface normal and a pass energy for narrow scan spectra of 20 eV at an instrument resolution of ~ 700 meV. Spectral analysis was performed using Casa XPS analysis software, and all spectra were calibrated by adjusting C 1s core level position to 284.8 eV.

Wafer cleaning, functionalization, and electrode fabrication

Experimental procedures are described in detail in the electronic supplementary material (ESM) (wafer cleaning, wafer functionalization, and electrode fabrication). Briefly, p-type, Zn-doped GaP(100) wafers were sonicated in acetone and isopropanol for 5 min each, followed by drying under nitrogen. Samples were exposed to an air-generated oxygen plasma at 30 W for 2 min, immersed in buffered hydrofluoric acid (6:1 HF/NH_4F in H_2O) for 5 min, followed by rinsing with Milli-Q water and methanol and

then drying under nitrogen. Freshly etched wafers were functionalized with porphyrin complexes by exposing the wafers to an argon-sparged solution containing a selected metalloporphyrin (1 mM) in toluene and illuminating with 254 nm UV light for 2 h. After rinsing with toluene, sonicating in dichloromethane, and washing with isopropanol, the modified wafers were dried and stored under vacuum. GaP working electrodes were fabricated by applying an indium-gallium eutectic (Aldrich) to the backside of a wafer, and then fixing a copper wire to the back of the wafer using a conductive silver epoxy (AI Technology). The copper wire was passed through a glass tube, and the wafer was insulated and attached to the glass tube with Loctite 615 Hysol Epoxy-patch adhesive. The epoxy was allowed to fully cure before any measurements.

Electrochemistry

Cyclic voltammetry was performed with a BioLogic SP-200 or SP-300 potentiostat using a glassy carbon (3 mm diameter) disk working electrode, a platinum counter electrode, and a silver wire pseudoreference electrode in a conventional three-electrode cell at a scan rate of 500 mV s^{-1}. Dichloromethane or butyronitrile (Aldrich) were used as solvents for electrochemical measurements. The supporting electrolyte was 0.1 M tetrabutylammonium hexafluorophosphate ($TBAPF_6$), and all solutions were sparged with argon. The working electrode was cleaned between experiments by polishing with alumina (50 nm diameter) slurry, followed by solvent rinses. The concentration of all homogeneous porphyrin solutions was 0.34 mM.

Photoelectrochemistry

Photoelectrochemical (PEC) measurements were performed using 100 mW cm^{-2} illumination from a 100 W Oriel Solar Simulator equipped with an AM 1.5 filter. Linear sweep voltammetry was performed with a BioLogic SP-300 potentiostat using a platinum coil counter electrode, a Ag/AgCl, NaCl (3 M) reference electrode (0.21 V vs NHE), and GaP working electrodes, including GaP electrodes following buffered HF treatment as well as free-base-, iron-, cobalt-, nickel-, copper-, and zinc- porphyrin-modified GaP (abbreviated in this report as H_2P|GaP, FeP|GaP, CoP|GaP, NiP|GaP, CuP|GaP, and ZnP|GaP, respectively), in a modified cell containing a quartz window. The supporting electrolyte was 0.1 M phosphate buffer (pH 7), and a minimum of three individual wafers were tested for each GaP working electrode sample. Linear sweep voltammograms were recorded at a sweep rate of 100 mV s^{-1} under a continuous flow of 5% hydrogen in nitrogen. V_{oc} and J_{sc} were determined from the applied potential at the zero-current value and current density at 0 V vs RHE on the linear sweep voltammograms, respectively. P_{max} was taken as the maximum value of the product of the applied potential (V vs RHE) and current density. *ff* was determined by dividing P_{max} by the product of V_{oc} and J_{sc}.

Gas chromatography

Detection of hydrogen gas was performed via gas chromatography using an Agilent 490 Micro GC equipped with a 5 Å Mol-Sieve column at a temperature of 80 °C and argon as the carrier gas. Gas samples were syringe injected using 5 mL aliquots of headspace gas collected with a gas-tight Hamilton syringe from a sealed PEC cell both prior to and following 46 min of constant-potential photoelectrolysis. In these experiments, the working electrodes were polarized at − 0.610 V vs Ag/AgCl, NaCl (3 M), slightly positive of 0 V vs RHE, where $E_{vs\ RHE} = E_{vs\ Ag/AgCl} + (0.05916\ V)(pH) + 0.21\ V$. Prior to the experiment, the cell was purged for 30 min with argon before sealing. The retention time of hydrogen was confirmed using a known source of hydrogen obtained from a standard lecture bottle containing a hydrogen and nitrogen mixture.

Results and discussion

Synthesis of metalloporphyrin complexes

The synthetic strategy used to prepare the target metalloporphyrin complexes (abbreviated in this report as FeP-Styr, CoP-Styr, NiP-Styr, CuP-Styr, and ZnP-Styr, respectively) is depicted in Fig. 1. NiP-Styr, CuP-Styr, and ZnP-Styr were synthesized using methods similar to those reported for the Fe and Co analogs (Khusnutdinova et al. 2017). In summary, 5,10,15,20-tetra-*p*-tolylporphyrin (TTP) was prepared via condensation of pyrrole and *p*-tolualdehyde according to the method reported by Adler et al. (1967). The resulting porphyrin complex was brominated at the β-position of the macrocycle using *N*-bromosuccinimide in a mixture of chloroform and pyridine to afford 2-bromo-5,10,15,20-tetra-*p*-tolylporphyrin (BrTTP). Cross coupling of the bromoporphyrin complex with 4-vinylphenylboronic acid was then used to prepare 2-(4-vinylphenyl)-5,10,15,20-tetra-*p*-tolylporphyrin (H_2P-Styr). Finally, H_2P-Styr was treated with acetate or chloride salts of Fe(III), Co(II), Ni(II), Cu(II), or Zn(II) to obtain the target compounds (FeP-Styr, CoP-Styr, NiP-Styr, CuP-Styr, or ZnP-Styr, respectively). Further details on the synthesis and characterization of all compounds used in these studies, including structural characterization via MALDI-TOF mass spectrometry, ^{1}H NMR spectroscopy, and FTIR spectroscopy, are included in the ESM.

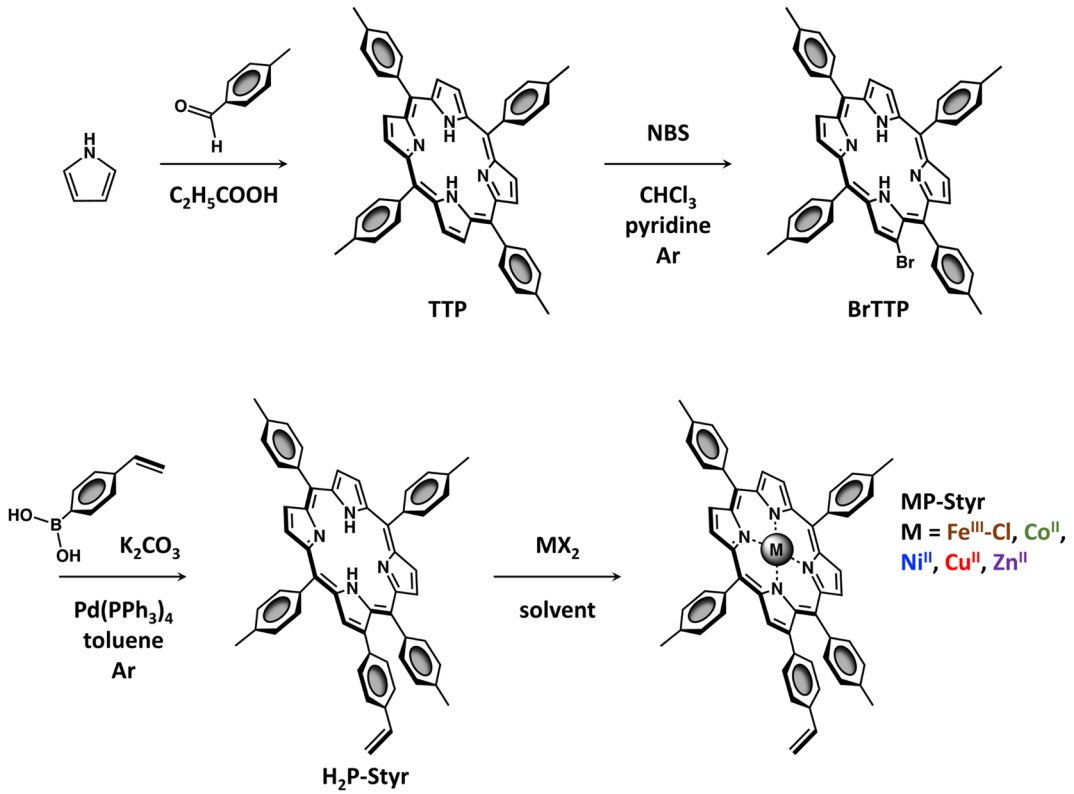

Fig. 1 Synthetic scheme used to prepare metalloporphyrin complexes bearing a 4-vinylphenyl surface-attachment group

Optical and electrochemical properties of the homogeneous metalloporphyrin complexes

Figure 2 shows normalized UV–Vis absorption spectra of the homogeneous metalloporphyrin complexes recorded in dichloromethane. Each spectrum displays a relatively high-energy absorption band, associated with Soret-absorption bands, and lower energy absorption features, associated with Q-absorption bands (Valicsek and Horváth 2013). Maxima for the Soret-absorption band of NiP-Styr, CuP-Styr, and ZnP-Styr are centered at 422 nm, 420 nm, and 424 nm, respectively, and the most intense Q-absorption band of each complex is centered at 535 nm, 543 nm, and 552 nm, respectively. As compared with the corresponding metallo-analogs of 5,10,15,20-tetra-*p*-tolylporphyrins (i.e. model Fe, Co, Ni Cu, and Zn metalloporphyrin complexes featuring an H atom in place of the vinylphenyl moiety, which are abbreviated in this report as FeTTP, CoTTP, NiTTP, CuTTP, and ZnTTP), the vinylphenyl-containing complexes display bathochromic shifts of both their Soret- and Q-absorption bands as well as relatively lower ratios of their Soret- to Q-absorption band intensities (Table 1 and Fig. S7). The bathochromic shifts of these bands are ascribed in part to nonplanar deformations of the porphyrin macrocycle caused by replacing the H atom with the bulkier vinylphenyl substituent. This bulkier group distorts the porphyrin macrocycle and destabilizes the highest occupied molecular orbital (HOMO), thereby lowering the energy of the π–π* transitions (Jentzen et al. 1995; Haddad et al. 2003). The diminished relative intensities of Soret-absorption bands are also consistent with theoretical predictions indicating that ruffling of porphyrin macrocycles decreases the oscillator strengths of Soret-absorption bands, yet the oscillator strengths of Q-absorption bands remain relatively unperturbed (Jentzen et al. 1995).

The electrochemistry of all homogeneous metalloporphyrin complexes described in this report were studied via cyclic voltammetry using argon-sparged solutions of the metalloporphyrins dissolved in dichloromethane or butyronitrile along with 0.1 M $TBAPF_6$ (Fig. 3). Under these conditions, voltammograms of NiP-Styr, CuP-Styr, and ZnP-Styr show chemically reversible and electrochemically quasi-reversible redox processes that are summarized in Table 2. This table includes information on the midpoint potentials ($^{n}E_{1/2}$, where n = i, ii, and iii are midpoint potentials for the first, second, and third redox couples observed at increasing anodic polarization, and n = I, II, and III are midpoint potentials for the first, second, and third redox couples observed at increasing cathodic polarization) and their peak-to-peak

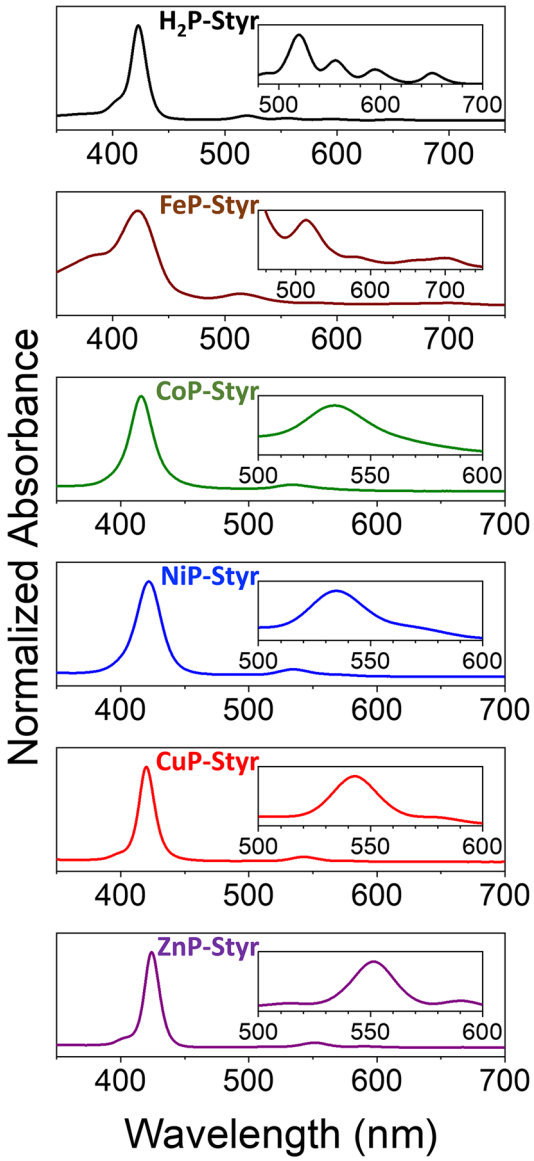

Fig. 2 Normalized UV–Vis absorption spectra of H_2P-Styr (black), FeP-Styr (brown), CoP-Styr (green), NiP-Styr (blue), CuP-Styr (red), and ZnP-Styr (purple) in dichloromethane. Insets show normalized Q-absorption band regions of the absorption spectra

separations (ΔE_p). By convention, all midpoint potentials are reported as reduction half reactions (Trasatti 1986). $^nE_{1/2}$ is estimated as the average of anodic and cathodic peak potentials for a given quasi-reversible redox couple. ΔE_p, which gives information on the degree of electrochemical reversibility, is reported as the difference between the anodic and cathodic peak potentials. Based on previous investigations of metalloporphyrins containing nickel, copper, or zinc, we tentatively assign all redox processes of NiP-Styr, CuP-Styr, and ZnP-Styr as macrocycle-centered electron-transfer reactions (Brown et al. 1973; Kadish and Van Caemelbecke 2003; Fang et al. 2014). For the related iron and

Table 1 Wavelengths of Soret- and Q-absorption bands of porphyrin complexes in dichloromethane

Compound	Soret-absorption band(s) (nm)	Q-absorption band(s) (nm)
H_2P-Styr	423	520, 556, 595, 651
TTP	419	516, 552, 592, 647
FeP-Styr	385[a], 422	514, 576, 666[a], 699
FeTTP	381, 418	511, 575, 661[a], 695
CoP-Styr	416	534
CoTTP	412	529
NiP-Styr	422	535
NiTTP	416	528
CuP-Styr	420	543
CuTTP	416	540
ZnP-Styr	424	552
ZnTTP	421	549

[a]This absorption feature appears as a shoulder

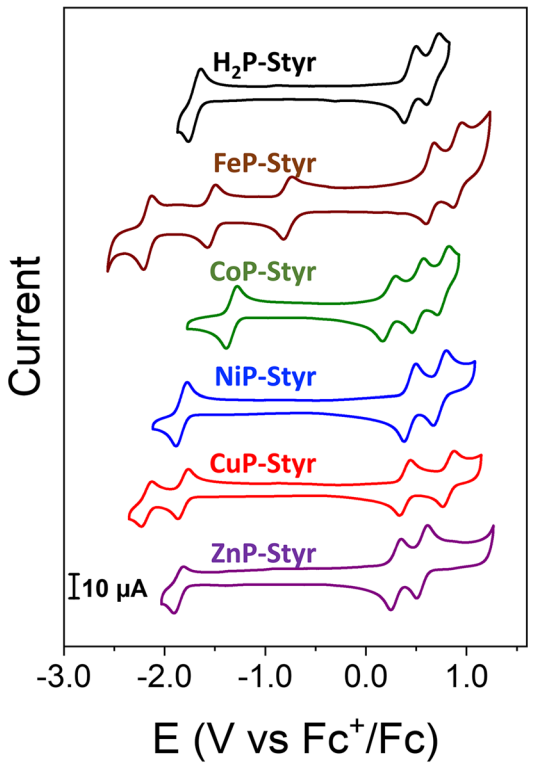

Fig. 3 Cyclic voltammograms recorded using samples of H_2P-Styr (black), FeP-Styr (brown), CoP-Styr (green), NiP-Styr (blue), CuP-Styr (red), and ZnP-Styr (purple) and a 3 mm glassy carbon working electrode and at a scan rate of 500 mV s^{-1}. The voltammogram of FeP-Styr was recorded using butyronitrile containing 0.1 M $TBAPF_6$ as a supporting electrolyte, and those of the other compounds were recorded using dichloromethane containing 0.1 M $TBAPF_6$ as a supporting electrolyte

cobalt complexes, metal-centered reduction processes may occur (Ke et al. 2018; Dalle et al. 2019). However, distinguishing macrocycle-centered redox processes from those that are metal-centered can be difficult and in some cases ambiguous.

For NiP-Styr, CuP-Styr, and ZnP-Styr, the values of $^{I}E_{1/2}$ are similar (within 4 mV) to those recorded using the corresponding model complexes without the 4-vinylphenyl substituent (Fig. S8, S10 and Table 2). Conversely, the $^{I}E_{1/2}$ of FeP-Styr is ~ 10 mV more cathodic than the $^{I}E_{1/2}$ of FeTTP, whereas the $^{I}E_{1/2}$ of CoP-Styr is ~ 40 mV more anodic than the $^{I}E_{1/2}$ of CoTTP. The relatively negligible effect of the 4-vinylphenyl substituent group on the $^{I}E_{1/2}$ of the Ni, Cu, and Zn complexes is consistent with theoretical predictions indicating the energies associated with the unoccupied π* orbitals of porphyrins are approximately unchanged by ruffling caused by the presence of substituents on the periphery of porphyrin macrocycles (Jentzen et al. 1995). The larger shifts of $^{I}E_{1/2}$ observed in Fe and Co complexes may be due to the enhanced metal-centered nature of the electron-transfer processes associated with these complexes (Kadish and Van Caemelbecke 2003). In contrast to $^{I}E_{1/2}$, the values of $^{i}E_{1/2}$ for FeP-Styr, CoP-Styr, NiP-Styr, and CuP-Styr are shifted cathodically (40–120 mV) with respect to their metallo-TTP analogs. These cathodic shifts are ascribed in part to a distortion of the porphyrin ring caused by the 4-vinylphenyl substituent, consistent with theoretical studies showing that bulky substituent groups distort the porphyrin macrocycle and destabilize the energy level of the HOMO (Haddad et al. 2003; Kadish and Van Caemelbecke 2003). However, the $^{i}E_{1/2}$ of ZnP-Styr, a d^{10} complex, is shifted anodically by ~ 10 mV.

Photoelectrochemical properties of the hybrid metalloporphyrin-modified GaP semiconductors

The FeP-Styr, CoP-Styr, NiP-Styr, CuP-Styr, and ZnP-Styr complexes were grafted onto GaP(100) surfaces utilizing the UV-induced immobilization chemistry of alkenes (Cicero et al. 2000; Li et al. 2009; Richards et al. 2010; Wang et al. 2010; Moore and Sharp 2013; Khusnutdinova et al. 2017) to yield samples of FeP|GaP, CoP|GaP, NiP|GaP, CuP|GaP, and ZnP|GaP (Fig. 4). Structural characterization of the resulting hybrid, heterogeneous-homogeneous assemblies, including XPS and contact angle measurements, are included in the ESM. Photovoltaic performance parameters were determined via analysis of current–voltage responses recorded using the metalloporphyrin-modified GaP working electrodes under simulated air mass 1.5 solar illumination. In these studies, all electrodes were characterized in pH-neutral aqueous solutions (0.1 M phosphate buffer) using a three-electrode cell configuration consisting of a GaP working electrode wired to appropriate counter and reference electrodes (see Materials and methods for details). Figure 5a displays linear sweep voltammograms recorded using either FeP|GaP, CoP|GaP, NiP|GaP, CuP|GaP, or ZnP|GaP working electrodes. The metalloporphyrin-modified GaP working electrodes display enhanced photoelectrochemical performance as compared to unmodified GaP working electrodes (Fig. S13); however, the overall current–voltage responses are unique for each metalloporphyrin-modified electrode (Table 3). All of the electrodes display relatively close values of J_{sc} (~ − 1.2 mA cm^{-2}), consistent with these limiting currents being set by the available photon flux and light-harvesting properties of the underpinning GaP semiconductor (Wadsworth et al. 2019). Conversely, the values of V_{oc} span from 0.61 to 0.73 V vs RHE across the series of metalloporphyrin-modified GaP electrodes. The V_{oc} gives a

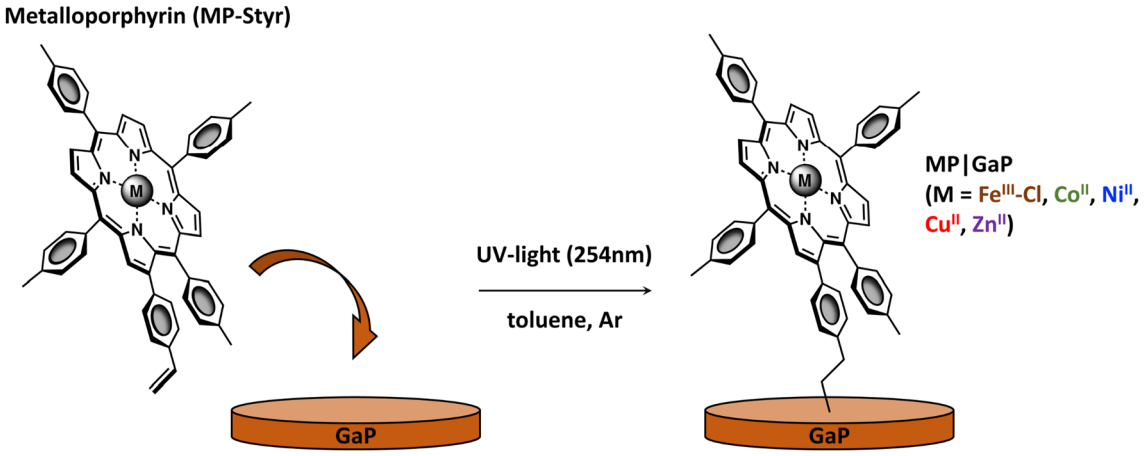

Fig. 4 Schematic representation of the UV-induced immobilization of metalloporphyrin complexes onto the GaP(100) surface to prepare metalloporphyrin-modified GaP electrodes (MP|GaP)

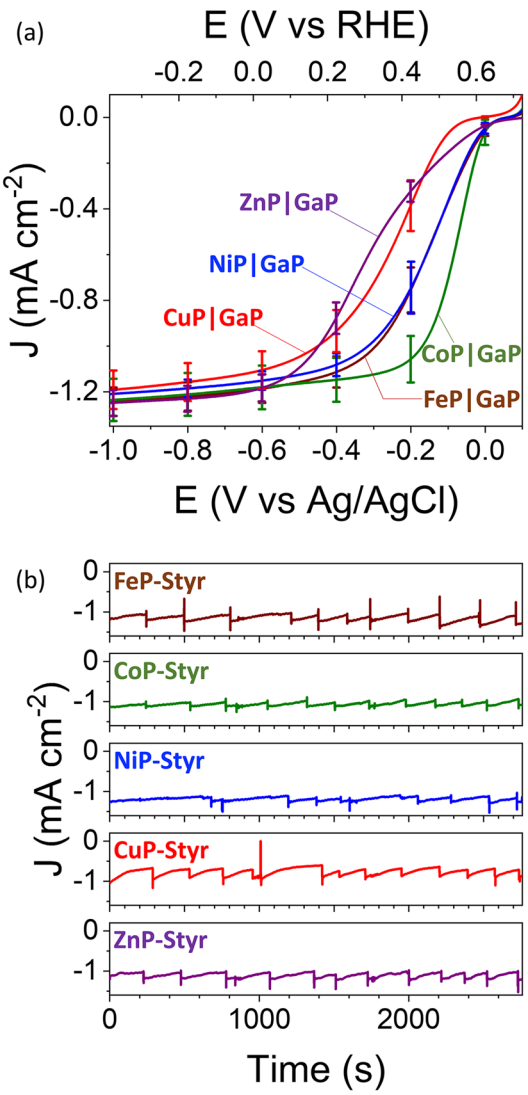

Fig. 5 **a** Linear sweep voltammograms and **b** plots of current density versus time for representative constant-potential photoelectrolysis experiments recorded using samples of FeP|GaP (brown), CoP|GaP (green), NiP|GaP (blue), CuP|GaP (red), and ZnP|GaP (purple) working electrodes in phosphate buffer (pH 7) under simulated air mass 1.5 solar illumination (100 mW cm^{-2}). Linear sweep voltammograms were recorded under a continuous flow of 5% hydrogen in nitrogen. Constant-potential photoelectrolysis experiments were recorded at an applied potential of 0.01 V vs RHE under argon containing 5 mL of methane

measure of the photovoltage, which is the degree of splitting between the electron and hole quasi-Fermi levels determined by the illumination intensity, flat-band potential, and presence of Fermi-level pinning (Lewis 1990; Walter et al. 2010; Joe et al. 2019). For the constructs presented in this article, CuP|GaP displays the most negative V_{oc}, and ZnP|GaP displays the most positive V_{oc}. More significant differences are observed in the *ff*, which is defined as P_{max} divided by the product of V_{oc} and J_{sc}. The *ff* is adversely affected by surface recombination of electrons/holes and uncompensated solution resistances. Even relatively small increases in *ff* can significantly alter the performance of a photoelectrochemical cell due to the comparative steep increase in photocurrent density produced by these changes (Lewis 1990; Walter et al. 2010). The largest *ff* of 0.57 is observed using CoP|GaP working electrodes, and the smallest *ff* of 0.21 is observed using ZnP|GaP working electrodes. The CuP|GaP working electrodes yield the least negative photocurrent densities under the applied potential range of 0.5–0.6 V vs RHE. However, due to the relatively higher *ff* of CuP|GaP, the current densities achieved by these constructs surpass those produced by ZnP|GaP at applied potentials more negative than ~ 0.46 V vs RHE and until the currents become limiting for both constructs at further negative potentials. The current–voltage curves recorded using FeP|GaP and NiP|GaP working electrodes are nearly identical, resulting in similar *ff* values of 0.42.

Constant-potential photoelectrolysis was performed using metalloporphyrin-modified GaP working electrodes polarized at potentials slightly positive of 0 V vs RHE (0.01 V vs RHE) in pH-neutral aqueous solutions over ~ 1 h of illumination. Under these conditions, all of the porphyrin-modified constructs display relatively stable photocurrent densities (Fig. 5b). The formation and dissolution of gas bubbles at the surface of the electrodes were also observed and correlated with relatively minor deviations in photocurrent intensities recorded over time. We interpret these deviations in terms of a lack of physical contact between the electrolyte solution and areas of the electrodes where hydrogen gas bubbles form. In the case of all constant-potential photoelectrolysis experiments, gas chromatography analysis of headspace gas samples taken from sealed PEC cells prior to and following ~ 1 h of illumination confirms the production of hydrogen.

Deviations in the shapes of the linear sweep voltammograms shown in Fig. 5a are most prominent at applied potentials between ~ 0.2–0.6 V vs RHE. In contrast to the current densities recorded at more negative biased potentials, the effects of charge recombination at these more positive potentials are anticipated to be further pronounced due to relatively lower band bending within the semiconductors (Peter 1990; Mills et al. 2014; Ilic et al. 2016). It has not escaped our attention that the *ff* values associated with the heterogeneous-homogeneous assemblies described in this report show a correlation with the values of $E_{1/2}$ measured for the related homogeneous metalloporphyrins (Fig. 6). These results indicate that functionalization of the GaP surface with a metalloporphyrin featuring less negative redox poise is correlated with a dampening of carrier-recombination kinetics as indicated

Table 2 Midpoint potentials ($^{n}E_{1/2}$) of porphyrin complexes as determined by cyclic voltammograms recorded in dichloromethane or butyronitrile and reported in V vs Fc^{+}/Fc with the corresponding peak-to-peak separations (ΔE_p) listed in parentheses and reported in mV

Compound	$^{III}E_{1/2}$	$^{II}E_{1/2}$	$^{I}E_{1/2}$	$^{i}E_{1/2}$	$^{ii}E_{1/2}$	$^{iii}E_{1/2}$
H_2P-Styr[a]			− 1.70 (124)	0.44 (121)	0.67 (125)	
TTP[a]			− 1.70 (100)	0.47 (101)		
FeP-Styr[b]	− 2.17 (83)	− 1.54 (80)	− 0.78 (80)	0.64 (81)	0.91 (88)	
FeTTP[b]	− 2.19 (75)	− 1.53 (80)	− 0.77 (65)	0.68 (84)	0.94 (111)	
CoP-Styr[a]			− 1.33 (107)	0.23 (132)	0.52 (116)	0.77 (118)
CoTTP[a]			− 1.37 (95)	0.35 (104)	0.55 (97)	0.80 (100)
NiP-Styr[a]			− 1.80 (111)	0.48 (118)	0.77 (129)	
NiTTP[a]			− 1.80 (85)	0.51 (90)	0.77 (105)	
CuP-Styr[a]		− 2.18 (108)	− 1.82 (104)	0.39 (109)	0.82 (114)	
CuTTP[a]		− 2.23 (101)	− 1.82 (92)	0.44 (98)	0.85 (104)	
ZnP-Styr[a]			− 1.86 (94)	0.30 (103)	0.56 (109)	
ZnTTP[a]			− 1.86 (88)	0.29 (91)	0.62 (95)	

[a]Recorded in 0.1 M $TBAPF_6$ in dichloromethane

[b]Recorded in 0.1 M $TBAPF_6$ in butyronitrile

Table 3 Photoelectrochemical parameters of GaP and metalloporphyrin-modified GaP working electrodes

Construct	Open-circuit voltage (V vs RHE)	Short-circuit current (mA cm^{-2})	Maximum power (mW cm^{-2})	Fill factor
GaP	0.70 ± 0.01	− 0.8 ± 0.3	0.12 ± 0.06	0.21 ± 0.04
FeP|GaP	0.688 ± 0.007	− 1.19 ± 0.06	0.34 ± 0.03	0.42 ± 0.03
CoP|GaP	0.679 ± 0.008	− 1.2 ± 0.1	0.46 ± 0.05	0.57 ± 0.01
NiP|GaP	0.681 ± 0.008	− 1.16 ± 0.04	0.33 ± 0.04	0.42 ± 0.03
CuP|GaP	0.610 ± 0.010	− 1.11 ± 0.08	0.24 ± 0.03	0.35 ± 0.03
ZnP|GaP	0.735 ± 0.002	− 1.19 ± 0.07	0.20 ± 0.02	0.23 ± 0.01

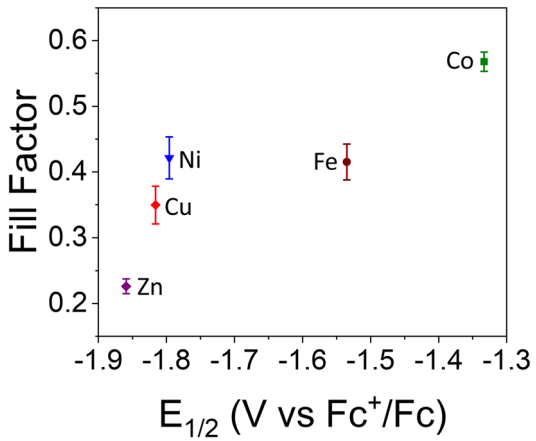

Fig. 6 Fill factors of metalloporphyrin-modified GaP photocathodes versus the 0/−1 midpoint potentials of the associated homogeneous metalloporphyrin complexes (MP-Styr, where M = Fe (brown), Co (green), Ni (blue), Cu (red), and Zn (purple)). $E_{1/2}$ represents $^{I}E_{1/2}$ of CoP-Styr, NiP-Styr, CuP-Styr, and ZnP-Styr recorded in dichloromethane or $^{II}E_{1/2}$ of FeP-Styr recorded in butyronitrile

by the increased *ff*. However, further studies are required to confirm the causation of this correlation and how well this trend holds when using an expanded selection of metalloporphyrin complexes, as these results could be due to multiple effects following surface modification, including changes of the band bending within the underpinning semiconductor (thermodynamics) as well as catalysis (kinetics). Nonetheless, the reported assemblies set the stage for better understanding charge-transfer and carrier-recombination kinetics at semiconductor|catalyst|liquid interfaces. In summary, chemical modification of GaP surfaces with the metalloporphyrin complexes described herein facilitates charge-transfer at semiconductor|catalyst|liquid interfaces and improves their photoelectrochemical performance.

Conclusion

We report the synthesis and characterization of metalloporphyrins containing a 4-vinylphenyl surface-attachment group at the β-position of the macrocycle and a first-row transition metal ion (Fe, Co, Ni, Cu, or Zn) at the center of the porphyrin macrocycle. Successful installment of the 4-vinylphenyl surface-attachment group and selected metal ion was confirmed by MALDI-TOF mass spectrometry, ^{1}H NMR spectroscopy, FTIR spectroscopy, UV–Vis absorption spectroscopy, and cyclic voltammetry. These complexes were grafted onto GaP(100) surfaces to create metalloporphyrin-modified photocathodes for driving the hydrogen evolution reaction. Linear sweep voltammograms recorded in pH-neutral aqueous solutions under simulated solar illumination show the metalloporphyrin-modified GaP electrodes display relatively similar values of J_{sc}, but significantly vary in their values of V_{oc} and *ff,* and display overall different wave-form shapes for their respective *J-V* curves. These results set the stage for better understanding structure–function relationships governing the performance of molecular-modified photoelectrodes, as well as strategies to optimizing their architectures and performance.

Supplementary Information The online version contains supplementary material available at https://doi.org/10.1007/s11120-021-00834-2.

Acknowledgements This work was supported by the National Science Foundation under Early Career Award 1653982 (polymeric surface chemistry) and by the U.S. Department of Energy, Office of Science, Office of Basic Energy Sciences, under Early Career Award DE-SC0021186 (analysis of recombination kinetics). G.F.M. acknowledges support from the Camille Dreyfus Teacher-Scholar Awards Program. B.L.W. was supported by an IGERT-SUN fellowship funded by the National Science Foundation (1144616) and the Phoenix Chapter of the ARCS Foundation. D.N. was supported by the Heiwa Nakajima Foundation. XPS data were collected at the Eyring Materials Center at Arizona State University. NMR studies were performed using the Magnetic Resonance Research Center at Arizona State University.

Author contributions The manuscript was written through contributions of all authors. All authors have given approval to the final version of the manuscript.

Funding This work was supported by the National Science Foundation under Early Career Award 1653982 (polymeric surface chemistry) and by the U.S. Department of Energy, Office of Science, Office of Basic Energy Sciences, under Early Career Award DE-SC0021186 (analysis of recombination kinetics). G.F.M. acknowledges support from the Camille Dreyfus Teacher-Scholar Awards Program. B.L.W. was supported by an IGERT-SUN fellowship funded by the National Science Foundation (1144616) and the Phoenix Chapter of the ARCS Foundation. D.N. was supported by the Heiwa Nakajima Foundation.

Declarations

Conflicts of interest The authors declare that they have no conflict of interest.

References

Adler AD, Longo FR, Finarelli JD, Goldmacher J, Assour J, Korsakoff L (1967) A simplified synthesis for meso-tetraphenylporphine. J Org Chem 32:476. https://doi.org/10.1021/jo01288a053

Ardo S, Fernandez Rivas D, Modestino MA, Schulze Greiving V, Abdi FF, Alarcon Llado E, Artero V, Ayers K, Battaglia C, Becker JP, Bederak D, Berger A, Buda F, Chinello E, Dam B, Di Palma V, Edvinsson T, Fujii K, Gardeniers H, Geerlings H, Hashemi SM, Haussener S, Houle F, Huskens J, James BD, Konrad K, Kudo A, Kunturu PP, Lohse D, Mei B, Miller EL, Moore GF, Muller J, Orchard KL, Rosser TE, Saadi FH, Schüttauf JW, Seger B, Sheehan SW, Smith WA, Spurgeon J, Tang MH, Van De Krol R, Vesborg PCK, Westerik P (2018) Pathways to electrochemical solar-hydrogen technologies. Energy Environ Sci 11:2768–2783. https://doi.org/10.1039/c7ee03639f

Beiler AM, Khusnutdinova D, Jacob SI, Moore GF (2016) Solar hydrogen production using molecular catalysts immobilized on gallium phosphide (111)A and (111)B polymer-modified photocathodes. ACS Appl Mater Interfaces 8:10038–10047. https://doi.org/10.1021/acsami.6b01557

Beiler AM, Khusnutdinova D, Wadsworth BL, Moore GF (2017) Cobalt porphyrin-polypyridyl surface coatings for photoelectrosynthetic hydrogen production. Inorg Chem 56:12178–12185. https://doi.org/10.1021/acs.inorgchem.7b01509

Beyene BB, Hung CH (2020) Recent progress on metalloporphyrin-based hydrogen evolution catalysis. Coord Chem Rev 410:213234. https://doi.org/10.1016/j.ccr.2020.213234

Brown GM, Hopf FR, Ferguson JA, Meyer TJ, Whitten DG (1973) Metalloporphyrin redox chemistry. The effect of extraplanar ligands on the site of oxidation in ruthenium porphyrins. J Am Chem Soc 95:5939–5942. https://doi.org/10.1021/ja00799a018

Cedeno D, Krawicz A, Doak P, Yu M, Neaton JB, Moore GF (2014) Using molecular design to control the performance of hydrogen-producing polymer-brush-modified photocathodes. J Phys Chem Lett 5:3222–3226. https://doi.org/10.1021/jz5016394

Cicero RL, Linford MR, Chidsey CED (2000) Photoreactivity of unsaturated compounds with hydrogen-terminated silicon(111). Langmuir 16:5688–5695. https://doi.org/10.1021/la9911990

Dalle KE, Warnan J, Leung JJ, Reuillard B, Karmel IS, Reisner E (2019) Electro- and solar-driven fuel synthesis with first row transition metal complexes. Chem Rev 119:2752–2875. https://doi.org/10.1021/acs.chemrev.8b00392

Fang Y, Senge MO, Van Caemelbecke E, Smith KM, Medforth CJ, Zhang M, Kadish KM (2014) Impact of substituents and nonplanarity on nickel and copper porphyrin electrochemistry: First observation of a Cu^{II}/Cu^{III} reaction in nonaqueous media. Inorg Chem 53:10772–10778. https://doi.org/10.1021/ic502162p

Faunce TA, Lubitz W, Rutherford AW, MacFarlane D, Moore GF, Yang P, Nocera DG, Moore TA, Gregory DH, Fukuzumi S, Yoon KB, Armstrong FA, Wasielewski MR, Styring S (2013) Energy and environment policy case for a global project on artificial photosynthesis. Energy Environ Sci 6:695–698. https://doi.org/10.1039/c3ee00063j

Gotico P, Halime Z, Aukauloo A (2020) Recent advances in metalloporphyrin-based catalyst design towards carbon dioxide reduction: From bio-inspired second coordination sphere modifications to hierarchical architectures. Dalton Trans 49:2381–2396. https://doi.org/10.1039/c9dt04709c

Haddad RE, Gazeau S, Pécaut J, Marchon JC, Medforth CJ, Shelnutt JA (2003) Origin of the red shifts in the optical absorption bands of nonplanar tetraalkylporphyrins. J Am Chem Soc 125:1253–1268. https://doi.org/10.1021/ja0280933

Ilic S, Brown ES, Xie Y, Maldonado S, Glusac KD (2016) Sensitization of p-GaP with monocationic dyes: the effect of dye excited-state

lifetime on hole injection efficiencies. J Phys Chem C 120:3145–3155. https://doi.org/10.1021/acs.jpcc.5b10474

Jentzen W, Simpson MC, Hobbs JD, Song X, Shelnutt JA, Ema T, Nelson NY, Medforth CJ, Smith KM, Veyrat M, Mazzanti M, Ramasseul R, Marchon JC, Takeuchi T, Goddard WA (1995) Ruffling in a series of Nickel(II) meso-tetrasubstituted porphyrins as a model for the conserved ruffling of the heme of cytochromes c. J Am Chem Soc 117:11085–11097. https://doi.org/10.1021/ja00150a008

Joe J, Yang H, Bae C, Shin H (2019) Metal chalcogenides on silicon photocathodes for efficient water splitting: A mini overview. Catalysts 9:149. https://doi.org/10.3390/catal9020149

Kadish KM, Van Caemelbecke E (2003) Electrochemistry of porphyrins and related macrocycles. J Solid State Electrochem 7:254–258. https://doi.org/10.1007/s10008-002-0306-3

Ke X, Kumar R, Sankar M, Kadish KM (2018) Electrochemistry and spectroelectrochemistry of cobalt porphyrins with π-extending and/or highly electron-withdrawing pyrrole substituents in situ electrogeneration of σ-bonded complexes. Inorg Chem. https://doi.org/10.1021/acs.inorgchem.7b02856

Khusnutdinova D, Beiler AM, Wadsworth BL, Jacob SI, Moore GF (2017) Metalloporphyrin-modified semiconductors for solar fuel production. Chem Sci 8:253–259. https://doi.org/10.1039/C6SC02664H

Krawicz A, Cedeno D, Moore GF (2014) Energetics and efficiency analysis of a cobaloxime-modified semiconductor under simulated air mass 1.5 illumination. Phys Chem Chem Phys 16:15818–15824. https://doi.org/10.1039/c4cp00495g

Lewis NS (1990) Mechanistic studies of light-induced charge separation at semiconductor/liquid interfaces. Acc Chem Res 23:176–183. https://doi.org/10.1021/ar00174a002

Li B, Franking R, Landis EC, Kim H, Hamers RJ (2009) Photochemical grafting and patterning of biomolecular layers onto TiO_2 thin films. ACS Appl Mater Interfaces 1:1013–1022. https://doi.org/10.1021/am900001h

McKone JR, Marinescu SC, Brunschwig BS, Winkler JR, Gray HB (2014) Earth-abundant hydrogen evolution electrocatalysts. Chem Sci 5:865–878. https://doi.org/10.1039/c3sc51711j

Mills TJ, Lin F, Boettcher SW (2014) Theory and simulations of electrocatalyst-coated semiconductor electrodes for solar water splitting. Phys Rev Lett 112:1–5. https://doi.org/10.1103/PhysRevLett.112.148304

Moore GF, Sharp ID (2013) A noble-metal-free hydrogen evolution catalyst grafted to visible light-absorbing semiconductors. J Phys Chem Lett 4:568–572. https://doi.org/10.1021/jz400028z

Peter LM (1990) Dynamic aspects of semiconductor photoelectrochemistry. Chem Rev 90:753–769. https://doi.org/10.1021/cr00103a005

Richards D, Zemlyanov D, Ivanisevic A (2010) Assessment of the passivation capabilities of two different covalent chemical modifications on GaP(100). Langmuir 26:8141–8146. https://doi.org/10.1021/la904451x

Trasatti S (1986) The absolute electrode potential: an explanatory note (Recommendations 1986). J Electroanal Chem Interfacial Electrochem 209:417–428. https://doi.org/10.1016/0022-0728(86)80570-8

Valicsek Z, Horváth O (2013) Application of the electronic spectra of porphyrins for analytical purposes: the effects of metal ions and structural distortions. Microchem J 107:47–62. https://doi.org/10.1016/j.microc.2012.07.002

Vullev VI (2011) From biomimesis to bioinspiration: What's the benefit for solar energy conversion applications? J Phys Chem Lett 2:503–508. https://doi.org/10.1021/jz1016069

Wadsworth BL, Beiler AM, Khusnutdinova D, Reyes Cruz EA, Moore GF (2019) Interplay between light flux, quantum efficiency, and turnover frequency in molecular-modified photoelectrosynthetic assemblies. J Am Chem Soc 141:15932–15941. https://doi.org/10.1021/jacs.9b07295

Walter MG, Warren EL, McKone JR, Boettcher SW, Mi Q, Santori EA, Lewis NS (2010) Solar water splitting cells. Chem Rev 110:6446–6473. https://doi.org/10.1021/cr1002326

Wang X, Ruther RE, Streifer JA, Hamers RJ (2010) UV-induced grafting of alkenes to silicon surfaces: photoemission versus excitons. J Am Chem Soc 132:4048–4049. https://doi.org/10.1021/ja910498z

Zhang W, Lai W, Cao R (2017) Energy-related small molecule activation reactions: oxygen reduction and hydrogen and oxygen evolution reactions catalyzed by porphyrin- and corrole-based systems. Chem Rev 117:3717–3797. https://doi.org/10.1021/acs.chemrev.6b00299